Acta Pharmaceutica Sinica B 2022;12(3):1240−1253

Chinese Pharmaceutical Association
Institute of Materia Medica, Chinese Academy of Medical Sciences

Acta Pharmaceutica Sinica B

www.elsevier.com/locate/apsb
www.sciencedirect.com

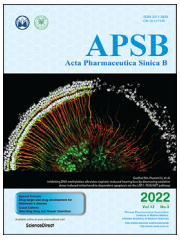

ORIGINAL ARTICLE

c-MYC-mediated TRIB3/P62^{+} aggresomes accumulation triggers paraptosis upon the combination of everolimus and ginsenoside Rh2

Min-Xia Su[a], Yu-Lian Xu[a], Xiao-Ming Jiang[a], Mu-Yang Huang[a], Le-Le Zhang[a], Luo-Wei Yuan[a], Xiao-Huang Xu[a], Qi Zhu[a], Jian-Li Gao[b], Jia-Hong Lu[a], Xiuping Chen[a], Ming-Qing Huang[c], Yitao Wang[a], Jin-Jian Lu[a,d,*]

[a]*State Key Laboratory of Quality Research in Chinese Medicine, Institute of Chinese Medical Sciences, University of Macau, Macao 999078, China*
[b]*School of Pharmaceutical Sciences, Zhejiang Chinese Medical University, Hangzhou 310000, China*
[c]*College of Pharmacy, Fujian University of Traditional Chinese Medicine, Fuzhou 350000, China*
[d]*MoE Frontiers Science Center for Precision Oncology, University of Macau, Macao 999078, China*

Received 17 June 2021; received in revised form 30 August 2021; accepted 31 August 2021

KEY WORDS

Everolimus;
Ginsenoside Rh2;
Paraptosis;
Aggresomes;
P62;
TRIB3;
c-MYC;
Lung cancer

Abstract The mammalian target of rapamycin (mTOR) pathway is abnormally activated in lung cancer. However, the anti-lung cancer effect of mTOR inhibitors as monotherapy is modest. Here, we identified that ginsenoside Rh2, an active component of *Panax ginseng* C. A. Mey., enhanced the anti-cancer effect of the mTOR inhibitor everolimus both *in vitro* and *in vivo*. Moreover, ginsenoside Rh2 alleviated the hepatic fat accumulation caused by everolimus in xenograft nude mice models. The combination of everolimus and ginsenoside Rh2 (labeled Eve-Rh2) induced caspase-independent cell death and cytoplasmic vacuolation in lung cancer cells, indicating that Eve-Rh2 prevented tumor progression by triggering paraptosis. Eve-Rh2 up-regulated the expression of c-MYC in cancer cells as well as tumor tissues. The increased c-MYC mediated the accumulation of tribbles homolog 3 (TRIB3)/P62^{+} aggresomes and consequently triggered paraptosis, bypassing the classical c-MYC/MAX pathway. Our study offers a potential effective and safe strategy for the treatment of lung cancer. Moreover, we have identified a new mechanism of TRIB3/P62^{+} aggresomes-triggered paraptosis and revealed a unique function of c-MYC.

*Corresponding author. Tel.: +853 88224674; fax: +853 28841358.
E-mail address: jinjianlu@um.edu.mo (Jin-Jian Lu).

Peer review under responsibility of Chinese Pharmaceutical Association and Institute of Materia Medica, Chinese Academy of Medical Sciences.

https://doi.org/10.1016/j.apsb.2021.09.014

1. Introduction

The mammalian target of rapamycin (mTOR) functions as an essential downstream effector of multiple oncogenes, including RAS and epidermal growth factor receptor (EGFR)[1,2]. The mTOR signaling pathway is frequently mutated and abnormally activated in lung cancer[3]. Everolimus (Eve), a first-generation mTOR inhibitor, is approved by the U.S. Food and Drug Administration for the treatment of several solid tumors, including breast cancer, advanced renal cancer and pulmonary neuroendocrine tumors[1]. Currently, more than 30 clinical trials of Eve against lung cancer have been registered on ClinicalTrials. gov by the U.S. National Library of Medicine. However, the anti-lung cancer effect of the Eve monotherapy is modest[4]. The median overall survival and the median progression-free survival are 6.7 and 1.3 months, respectively, in the Eve treatment group (NCT00374140). The adverse events of Eve, including anemia (22.5%), metabolism and nutrition disorders (10%), neutropenia (32.5%), dyspnea and pneumonitis (7.5%), frequently happen. High triglycerides or hypertriglyceridemia and hepatotoxicity or elevated liver enzymes in blood have also been observed in patients treated with Eve[5], highlighting the necessity of improving the efficiency and reducing the toxicity of Eve.

Ginseng (*Panax ginseng* C. A. Mey.), one of the most famous tonic, is widely used as a cancer treatment option[6] and has been recorded as a complementary and alternative medicine by the National Center for Complementary and Integrative Health (China)[7]. Ginseng improves physical stamina, stimulates immune function, and relieves various other health problems, such as respiratory and cardiovascular disorders[8]. Ginsenosides are the main bioactive components of ginseng, many of which show immunomodulatory and anti-cancer activities[9,10]. Ginsenoside Rh2 (Rh2) presents anti-cancer effects in various solid tumors, including lung cancer, breast cancer, ovarian cancer, prostate cancer and hematological tumors[7,8]. Rh2 has been recorded to induce cell cycle arrest and apoptosis, inhibit cell migration and reverse drug resistance[11]. Moreover, Rh2 acts on immune cells and regulates tumor microenvironment, thereby indirectly restraining tumor growth[12,13].

Paraptosis is a kind of programmed cell death characterized by cytoplasmic vacuolation, mitochondria and/or endoplasmic reticulum (ER) swelling, dependence on protein synthesis, caspase activation independence and lack of the typical hallmarks of apoptosis[14–16]. Paraptosis frequently undergoes cellular stress responses, including ER stress and oxidative stress[17,18]. A large number of unfolded or misfolded proteins in the rapidly growing tumor cells causes ER stress[19–21], suggesting that tumor cells may be more sensitive to agents that induce paraptosis than normal cells. This study has verified that the combination of Eve and Rh2 (labeled Eve-Rh2) shows remarkable anti-cancer effect *in vitro* and *in vivo*, which is mediated by the Eve-Rh2-induced paraptosis. The mechanical study suggests that Eve-Rh2 activates a unique function of c-MYC, through which Eve-Rh2 up-regulates the expression of tribbles homolog 3 (TRIB3), thereby mediating the accumulation of TRIB3/P62^{+} aggresomes and ultimately triggering paraptosis.

2. Materials and methods

2.1. Reagents

Eve (purity>98%), z-VAD-FMK, MG-132, 10058-F4, and 10074-G5 were obtained from Selleck Chemicals (Houston, TX, USA). Rh2 (purity≥98%) used in the cell models was purchased from Chengdu Must Bio-Technology Co., Ltd. (Chengdu, China). Rh2 (purity≥98%) used in the animal models was purchased from Sichuan Victory Biological Technology Co., Ltd. (Chengdu, China). Chelerythrine (purity>98%) was purchased from the National Institutes for Food and Drug Control (Beijing, China). Actinomycin D (A-D), bafilomycin A1 and chloroquine were obtained from Sigma−Aldrich (St. Louis, MO, USA). Cycloheximide (CHX) was obtained from Cell Signaling Technology, Inc. (Beverly, MA, USA). Alanine aminotransferase (ALT) and aspartate aminotransferase (AST) test kits were provided by the Nanjing Jiancheng Bioengineering Institute (Nanjing, China). The hematoxylin and eosin (H&E) staining kit, oil red O staining kit and lactate dehydrogenase (LDH) release assay kit were purchased from Beyotime Biotechnology (Shanghai, China).

2.2. Cell culture

Human EGFR-mutant lung cancer cell lines NCI-H1975 and HCC827 were obtained from Shanghai Cell Bank (Shanghai, China). The human A549 cell line (harboring the KRAS mutation) was purchased from the American Type Culture Collection (Rockville, MD, USA). The osimertinib resistant NCI-H1975/OSIR cell line was established in our laboratory[22]. Cells were maintained in Roswell Park Memorial Institute 1640 medium supplemented with 10% fetal bovine serum and 1% penicillin−streptomycin (Gibco, Carlsbad, CA, USA). All cells were incubated under 5% CO_2 at 37 °C.

2.3. Xenograft nude mice models

Five-week-old male BALB/c nude mice were provided by the specific-pathogen free Animal Facility of University of Macau and kept in the facility. All operations were approved by the Animal Ethics Committee of University of Macau. Human lung cancer NCI-H1975 (2×10^6) or HCC827 (3×10^6) cells were subcutaneously inoculated in the right back of each mouse. Five days after inoculation, the mice were randomly divided into four groups ($n = 8$) in accordance with the intragastric administration of the following treatments: G1, solvent control group; G2, Rh2 (5 mg/kg/day) group; G3, Eve (1 mg/kg/day) group; and G4, Eve-Rh2 group (1 mg/kg/day Eve + 5 mg/kg/day Rh2). All compounds were diluted in 0.9% saline solution. The dose of Eve was calculated according to the dosages used in clinical trials[23], while that of Rh2 was determined by the preliminary study and relevant literatures[24]. Tumor volume was calculated using Eq. (1):

$$\text{Tumor volume} = \text{Length} \times \text{Width}^2/2 \quad (1)$$

After 28 days of administration, the levels of fasting blood glucose of four mice from each group in NCI-H1975 and HCC827 mice models were tested by using the OneTouch Ultra Easy Glucometer (LifeScan Inc., Milpitas, CA, USA). Serum was obtained from each mouse, and the levels of ALT and AST were determined. Afterwards, the mice were sacrificed, and the tumors as well as the organs (*i.e.*, livers and kidneys) were dissected. The tumors were imaged. The pathologic changes in organs were observed using the H&E staining assay, the lipid droplets in the livers were observed using oil red O staining, and the expression level of c-MYC in tumors was analyzed using the immunohistochemical staining. The primary antibody against c-MYC (#ab32072) used in immunohistochemical staining was purchased from Abcam (Cambridge, UK).

2.4. MTT assay and LDH release assay

Cells were treated as indicated and incubated with the prepared 1 mg/mL tetrazolium salt MTT solution (Sigma−Aldrich). Afterwards, the MTT solution was discarded, and DMSO (Sigma−Aldrich) was added to dissolve the formazan crystals. The optical density at 570 nm was monitored. After treatment for 6 h, LDH release was determined using the LDH release assay kit according to the manufacturer's instructions. Absorbance at 490 nm was measured by the SpectraMax M5 microplate reader (Molecular Devices, Sunnyvale, CA, USA).

2.5. Cell morphology observation

Cells were treated as indicated, and the momentary cell morphology was captured using the Axiovert 200 inverted microscope (Zeiss, Oberkochen, Germany). The number of vacuolated cells was manually counted. The dynamic changes in the cell morphology after treatment were monitored using the IncuCyte S3 Live-Cell Analysis System (Essen BioScience Inc., Ann Arbor, MI, USA). Images were obtained every 20 min for 24 h.

2.6. Western blot

Cells were lysed using the RIPA lysis buffer (Beyotime Biotechnology). The dissolution agents for soluble and insoluble protein extraction were different. Cells were lysed by Triton-X100 in PBS and centrifuged to extract the soluble proteins in the supernatant. Sediments were dissolved in 1% sodium dodecyl sulfate to obtain the insoluble proteins. Equivalent protein samples were separated using the sodium dodecyl sulfate−polyacrylamide gel electrophoresis, and then proteins were transferred onto the polyvinylidene fluoride membranes. After blocking in 5% nonfat milk for 1 h, membranes were incubated with the indicated primary antibodies overnight at 4 °C and further incubated with the relative secondary antibodies. Afterwards, the membranes were exposed using the ECL Select Western blot detection reagent (GE Healthcare, Uppsala, Sweden). The primary antibodies against Alix (#2171), ubiquitin (#3933), BIP (#3177), CHOP (#2895), ATF4 (#11815), IRE1α (#3294), XBP1s (#12782), PERK (#5683), P-eIF2α (#3398), eIF2α (#5324), ATF6 (#65880), P62 (#8025), c-MYC (#5605), MAX (#4739), HSP90 (#5087), β-actin (#3700), and GAPDH (#5174), as well as the anti-rabbit and the anti-mouse IgG HRP-conjugated secondary antibodies were obtained from Cell Signaling Technology, Inc. (Beverly, MA, USA). The primary antibody against TRIB3 (#ab137526) was purchased from Abcam (Cambridge, UK).

2.7. RNA extraction and qRT-PCR

After treatment, cells were lysed using the TRIzol reagent (Invitrogen, Carlsbad, CA, USA). Total RNA was extracted using chloroform and isopropanol. The complementary DNA was synthesized using the Transcriptor First Strand cDNA Synthesis Kit (Thermo Fisher Scientific, Waltham, MA, USA). The SYBR Green Kit (Roche, Basel, Switzerland) was used to prepare the samples, and qRT-PCR assay was conducted in the ViiA 7 Real-Time PCR System (Applied Biosystems, Waltham, MA, USA). Primers are listed in Supporting Information Table S1. *GAPDH* was used as the internal control, and the relative expression levels of indicated genes were calculated by $2^{-\Delta\Delta Ct}$.

2.8. Immunofluorescence

After treatment, cells were fixed using 4% paraformaldehyde, permeabilized using 0.5% Triton X-100, blocked with 5% bovine serum albumin and incubated with indicated antibodies overnight at 4 °C. On the next day, the cells were incubated with the Alexa Fluor 594-conjugated or the Alexa Fluor 488-conjugated secondary antibody (Thermo Fisher Scientific) and further stained with Hoechst 33342. Then, the cells were imaged using the Leica TCS SP8 confocal microscope (Leica, Solms, Germany). The primary antibody against P62 (#18420-1-AP) was purchased from Proteintech Group, Inc. (Rosemont, IL, USA). The primary antibodies against TRIB3 and c-MYC were the same as those used in Western blot.

Aggresomes accumulation was detected using the Proteostat Aggresome Detection Kit (Enzo Life Sciences, Inc., Farmingdale, NY, USA) according to the manufacturer's instructions. Briefly, cells were fixed using 4% paraformaldehyde and permeabilized using 0.5% Triton X-100. Then, the cells were incubated with the Proteostat Aggresome dye for 1.5 h in the dark at room temperature and imaged using the Leica TCS SP8 confocal microscope (Leica).

2.9. Proteasome-Glo chymotrypsin-like cell-based assay

The activity of the proteasome was determined by following the manufacturer's instructions. Briefly, compound solutions were removed after treatment. New medium and the isopycnic Proteasome-Glo Cell-Based Reagents (Promega Corporation, Madison, WI, USA) were added to each well. The fluorescence intensity was measured using the PerkinElmer microplate reader (PerkinElmer, Wellesley, MA, USA). Relative activity of the proteasome was normalized to the control level.

2.10. RNA-Seq analysis

Cells were treated for 6 h, and the total RNA was extracted using the TRIzol reagent. RNA-Seq was conducted by the Omigen (Hangzhou, China) through the Illumina HiSeq X Ten PE150 Sequencing System. Differentially expressed genes were identified through the differential gene expression algorithm in the Partek Genomics Suite. The genes showing more than two-fold changes and $P < 0.05$ were considered as differentially expressed genes. The top 100 differentiated genes sorting by P value are

listed in Supporting Information Table S2. Gene Ontology analysis was performed to enrich the biological process in accordance with the database (http://www.geneontology.org/). Ingenuity Pathway Analysis (IPA) was performed to analyze the upstream regulators and the regulatory network on the basis of the Ingenuity Knowledge Base Library.

2.11. Luciferase assay

The pMYC-TA-luc plasmid (Beyotime Biotechnology) was used to determine the transcriptional activity of c-MYC, which contained several E-box DNA binding elements. The pMYC-TA-luc plasmid or the negative control plasmid and the TurboFect Transfection Reagent (Thermo Fisher Scientific) were transferred to the cells by following the instructions. Cells were treated as indicated for 6 h and lysed using the lysis buffer. The Luciferase Assay Reagent II was added to the cell lysates by following the instructions of the Dual-Luciferase Reporter Assay System (Promega Corporation). The bioluminescence was measured using the 1420 Multilabel Counter Victor3 Microplate Reader (PerkinElmer).

2.12. Small interfering RNA (siRNA) transfection

The specific or scrambled siRNA was transfected into cells following the manufacturer's instructions by using the Lipofectamine 2000 Transfection Reagent (Invitrogen)[25]. The sequences of siRNA are listed in Table S1. Two c-MYC specific siRNAs with different sequences were used together to silence the expression of c-MYC.

2.13. Transmission electron microscopy

After treatment, cells were fixed by using 2.5% glutaraldehyde at room temperature in dark. Transmission electron microscopy analysis was performed by Wuhan Servicebio Technology Co., Ltd. (Wuhan, China) through the HT7700 Transmission Electron Microscope (Hitachi High-Tech Corporation, Tokyo, Japan).

2.14. Statistical analysis

The *in vitro* data were presented as mean ± standard deviation (SD), whereas the *in vivo* data were presented as mean ± standard error of mean (SEM) due to the individual difference of animals. All presented *in vitro* experiments were repeated three times at least. Significance was analyzed using the GraphPad Prism 6.0 (GraphPad Software Inc., San Diego, CA, USA) through one-way ANOVA or two-tailed Student's *t* test. $*P < 0.05$ and $**P < 0.01$ are considered statistically significant, whereas the ns stands for not statistically significant.

3. Results

3.1. Eve-Rh2 shows potential anti-lung cancer effect in vitro and in vivo

Our preliminary study showed that the combination of Eve (10 μmol/L) and Rh2 (10 μmol/L) remarkably triggered cell death in lung cancer cells. Afterwards, cancer cells were treated with the combination of Eve and Rh2 by using various treatment sequences, including pretreatment with Eve, pretreatment with Rh2, and concurrent treatment (Supporting Information Fig. S1A). The strongest anti-cancer effect *in vitro* was obtained in the group of co-treatment with Rh2 after the Eve pretreatment for 1 h (Fig. S1B), which was labeled as Eve-Rh2 and was chosen as the treatment manner in the following study. Herein, cell survival of the four human lung cancer cell lines (NCI-H1975, NCI-H1975/OSIR, HCC827, and A549) was tested under Rh2 (10 μmol/L), Eve (10 μmol/L), and Eve-Rh2 treatments for 24 h. Both Rh2 and Eve monotreatments induced a slight cytotoxicity in all tested cell lines (Fig. 1A), presumably because of the low concentration and short treatment time[8,26]. However, Eve-Rh2 triggered significant cell death within 24 h with cell inhibitory rates of 78.24 ± 8.74% in NCI-H1975, 66.56 ± 11.42% in NCI-H1975/OSIR, 54.80 ± 12.83% in HCC827 and 55.44 ± 4.73% in A549 (Fig. 1A). Meanwhile, the Eve-Rh2 treatment caused the formation of uneven-sized vacuoles in all tested cell lines (Fig. 1B). The anti-cancer effect of Eve-Rh2 was further evaluated in nude mice models by subcutaneously injecting NCI-H1975 or HCC827 cancer cells. Eve-Rh2 significantly suppressed tumor growth, and the anti-cancer effect of Eve-Rh2 treatment showed significant advantage over both Rh2 and Eve monotreatments (Fig. 1C−H). Eve monotreatment has been reported to cause hepatic steatosis in clinical case and hepatotoxicity in clinical trials[27,28]. In our study, about 30% livers in Eve treatment group exhibited pale spots in appearance (Supporting Information Fig. S2A and S2B), whereas the serum ALT and AST were not elevated after Eve treatment (Supporting Information Fig. S3). Nevertheless, small vacuoles were observed in the hepatocytes around the nucleus as shown by H&E staining (Fig. S2C and S2D), and lipid droplets in livers were demonstrated by oil red O staining (Fig. S2E and S2F), which was used for fat droplet identification[29,30], indicating that Eve causes hepatic fat accumulation. In contrary, all livers in the Eve-Rh2-treated mice were healthy and as normal as untreated mice as evidenced by the appearance, H&E staining and oil red O staining (Fig. 1K, L and Fig. S2), suggesting that Rh2 attenuates Eve-caused hepatic fat accumulation. In addition, Eve-Rh2 treatment did not cause any injury to kidney, the primary organ of excretion[31], as shown in histological sections (Fig. 1K and L), and the body weight of the mice in all groups had no difference after relative administration (Fig. 1I and J), further indicating the reliable safety of Eve-Rh2 treatment *in vivo*.

3.2. Eve-Rh2 induces paraptosis in lung cancer cells

Thereafter, the type of cell death induced by Eve-Rh2 treatment was clarified. As shown in Fig. 2A and B, Eve-Rh2 induced caspases-independent cell death and did not trigger cell apoptosis (Supporting Information Fig. S4A). Bafilomycin A1 and chloroquine, which are autophagy inhibitors, did not reverse Eve-Rh2-induced cell death, even though the expression of LC3II was up-regulated by the Eve-Rh2 treatment (Fig. S4B−S4D). These data suggest that Eve-Rh2 caused neither apoptosis nor autophagic cell death. Then the IncuCyte S3 Live-Cell Analysis System was used to monitor the cell morphology regularly after Eve-Rh2 treatment (Fig. 2C). The formation of vacuoles was observed in cell cytosol after Eve-Rh2 treatment for 2 h. Increased cells vacuolized and ultimately died in a manner similar to balloon explosion. After Eve-Rh2

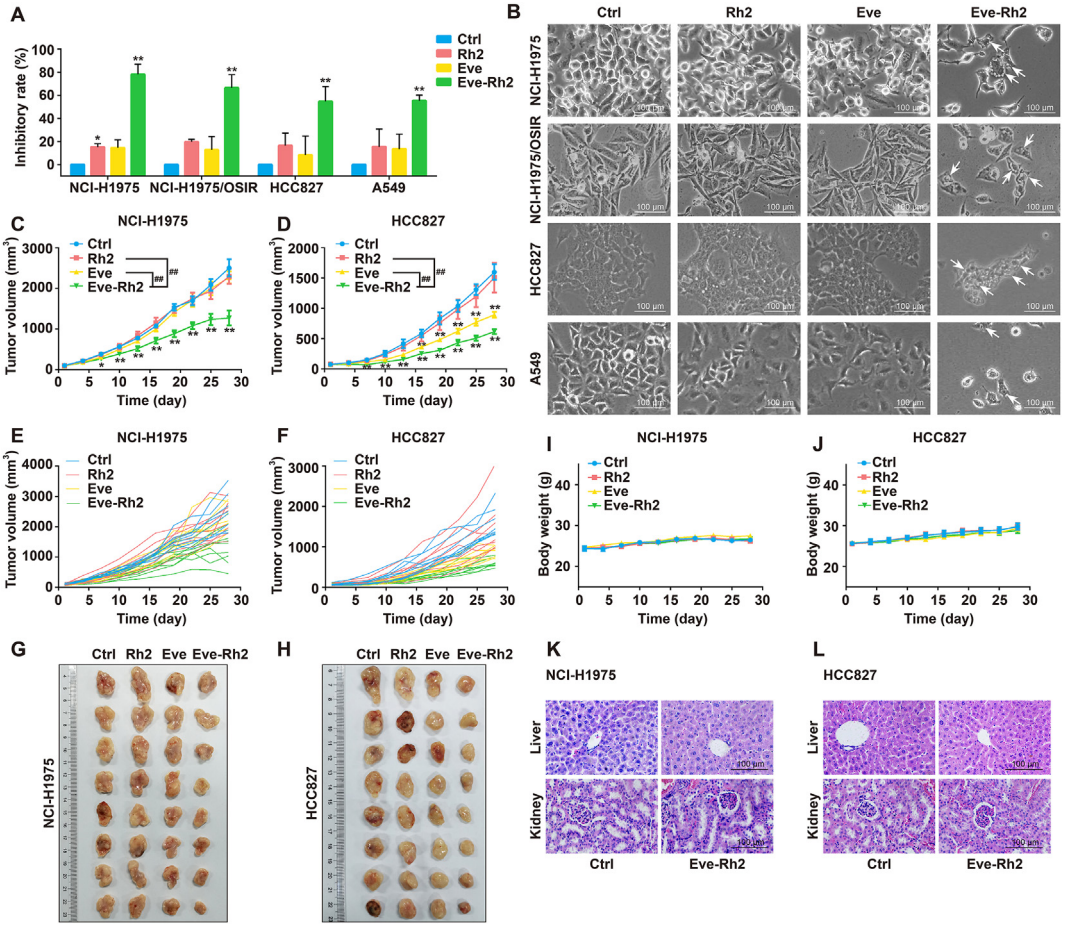

Figure 1 Eve-Rh2 showed significant anti-cancer effect *in vitro* and *in vivo*. NCI-H1975, NCI-H1975/OSIR, HCC827, and A549 cells were treated with Rh2 (10 μmol/L), Eve (10 μmol/L), or Eve-Rh2. (A) Cell viability was detected using MTT assay after 24 h treatment. Data represent mean ± SD, $n = 3$; $^{*}P < 0.05$ and $^{**}P < 0.01$ between the tagged group and ctrl group. (B) Cell morphology was imaged (scale bar = 100 μm) 24 h after treatment. White arrows were used to point out the cytoplasmic vacuoles. Nude mice were subcutaneously injected with NCI-H1975 or HCC827 cells. Five days later, the mice were gavaged with 0.9% NaCl, Rh2 (5 mg/kg/day), Eve (1 mg/kg/day), or Eve-Rh2 (1 mg/kg/day Eve + 5 mg/kg/day Rh2). (C) and (D) Tumor volumes during the administration period were presented as mean ± SEM, $n = 8$; $^{*}P < 0.05$ and $^{**}P < 0.01$ between the tagged group and ctrl group, and $^{\#\#}P < 0.01$ between the labelled group and Eve-Rh2 group. (E) and (F) Tumor volume of each mouse. (G) and (H) Representative tumors after the administration. (I) and (J) Body weights of mice were presented as mean weight ± SEM, $n = 8$. (K) and (L) Representative H&E-stained sections of livers and kidneys (400× magnification).

treatment for 6 h, the rough ER lesions were diffused, and the ER lumens were significantly expanded and vacuolated (Fig. 2D). Cytoplasmic vacuolation and ER swelling are regarded as the characteristics of paraptosis[15], which can be reversed by protein synthesis inhibitors[32]. In our study, both CHX (the translational inhibitor) and A-D (the transcriptional inhibitor) reversed the Eve-Rh2-mediated cell death (Fig. 2E), as well as the cytoplasmic vacuolation (Fig. 2F and G). A similar phenomenon was also observed in A549 and HCC827 cells (Fig. 2H). Moreover, Eve-Rh2 reduced the expression level of Alix (Fig. 2I), serving as an inhibitory protein of paraptosis[33]. Although Rh2 and Eve monotreatments were reported to induce caspase-independent cell death in cancer cells[34,35], they did not induce cell death and cytoplasmic vacuolation alone in our tested cells (Fig. 1A and B), presumably because of the low concentration used here. In short, Eve-Rh2-induced paraptosis in lung cancer cells possess the following characteristics: independence of caspases activity, cytoplasmic vacuolation, antagonism by CHX or A-D, and down-regulation of Alix.

3.3. *Eve-Rh2 mediates aggresomes accumulation and ER stress*

The Eve-Rh2-induced paraptosis could be attenuated by the co-treatment with CHX or A-D, whereas Eve-Rh2 suppressed the *de novo* protein synthesis instead of increasing it (Supporting Information Fig. S5A). Moreover, the cap-dependent translation was suppressed by Eve and Eve-Rh2 treatments (Fig. S5B) owing to the inhibitory effect of Eve on the mTOR signaling pathway (Fig. S5C). Apparently, Eve-Rh2 induced paraptosis independent of the protein synthesis. Alix can interact with the endosomal sorting complex required for transport III (ESCRT-III), resulting in the regulation of protein sorting[36]. Down-regulation of Alix may disturb the proteostasis and cause ER swelling by interfering with the function of the ESCRT-III[37,38]. Further study showed that Eve-Rh2 decreased the protein level of Alix without reducing its transcription level (Supporting Information Fig. S6A and S6B). The overexpression of Alix delayed but did not reverse Eve-Rh2-mediated paraptosis (Fig. S6C−S6F). The proteasome inhibitor, MG-132, reversed the Eve-Rh2-decreased Alix protein

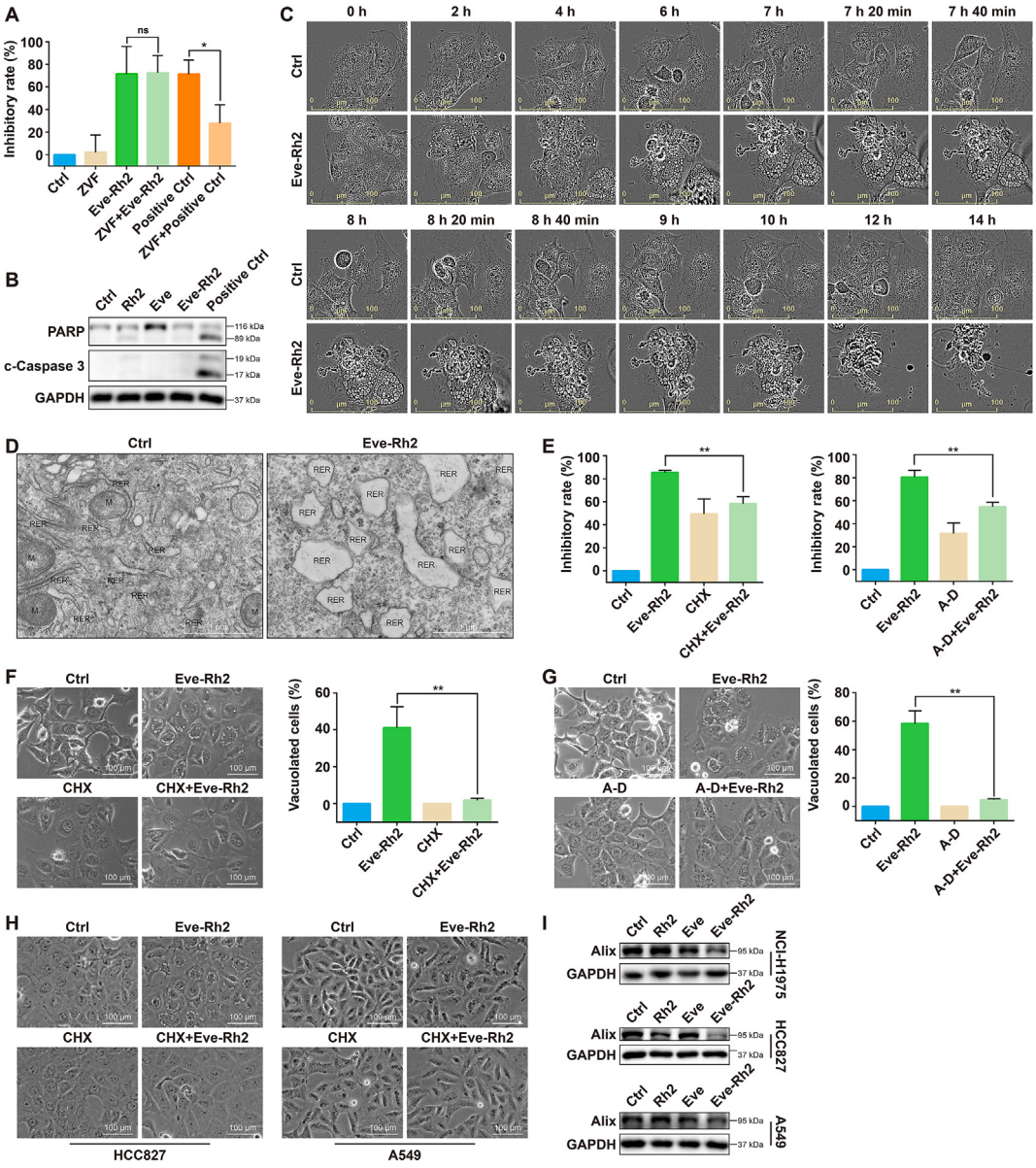

Figure 2 Eve-Rh2 induced paraptosis in lung cancer cells. (A) After co-treatment with z-VAD-FMK (ZVF, 20 μmol/L) and Eve (10 μmol/L) for 1 h, cells were further treated with Rh2 (10 μmol/L) for another 24 h, and the cell viability was detected using MTT assay. Chelerythrine (15 μmol/L) was used as the positive control of an apoptosis inducer. Data represent mean ± SD, $n = 3$; $^{*}P < 0.05$, ns stands for no statistical significance ($P > 0.05$). (B) Cells were treated with Rh2 (10 μmol/L), Eve (10 μmol/L), or Eve-Rh2 for 24 h or chelerythrine (15 μmol/L) for 3 h, and the expression levels of PARP and cleaved caspase 3 (c-caspase 3) were detected using Western blot. (C) NCI-H1975 cells were treated with Eve-Rh2 and monitored regularly through the IncuCyte S3 Live-Cell Analysis System. The representative pictures are shown. (D) After treated by Eve-Rh2 for 6 h, transmission electron microscopy was performed to observe the cytoplasmic vacuoles in NCI-H1975 cells. Rough endoplasmic reticulum (RER) and mitochondria (M) were pointed out. (E) NCI-H1975 cells were pretreated with cycloheximide (CHX, 40 μmol/L) or actinomycin D (A-D, 2 μg/mL) and Eve (10 μmol/L) for 1 h followed by the Rh2 (10 μmol/L) treatment. The cell viability was determined using MTT assay after 24 h treatment. Data represent mean ± SD, $n = 3$; $^{**}P < 0.01$. (F) and (G) Cell morphology was imaged (scale bar = 100 μm) after treatment for 6 h. The numbers of vacuolated and non-vacuolated cells were counted manually, and the ratio of vacuolated cells was calculated and shown as mean ± SD, $n = 3$; $^{**}P < 0.01$. (H) Morphological changes in HCC827 and A549 cells after pretreatment with CHX (40 μmol/L) and Eve (10 μmol/L) for 1 h and further treatment with Rh2 (10 μmol/L) for another 6 h (scale bar = 100 μm). (I) Protein level of Alix was detected using Western blot after treatment with Rh2 (10 μmol/L), Eve (10 μmol/L), or Eve-Rh2 for 6 h in NCI-H1975, A549, and HCC827 cells.

level (Fig. S6C) but dramatically enhanced the cytotoxicity of Eve-Rh2 treatment. Eve-Rh2 with MG-132 pretreatment induced significant cell death within 6 h (Fig. 3A and B, Supporting Information Fig. S7), indicating that Alix played a marginal role in the Eve-Rh2-induced paraptosis. Besides, Eve-Rh2 increased the level of ubiquitin (Fig. 3C). Eve-Rh2 caused the

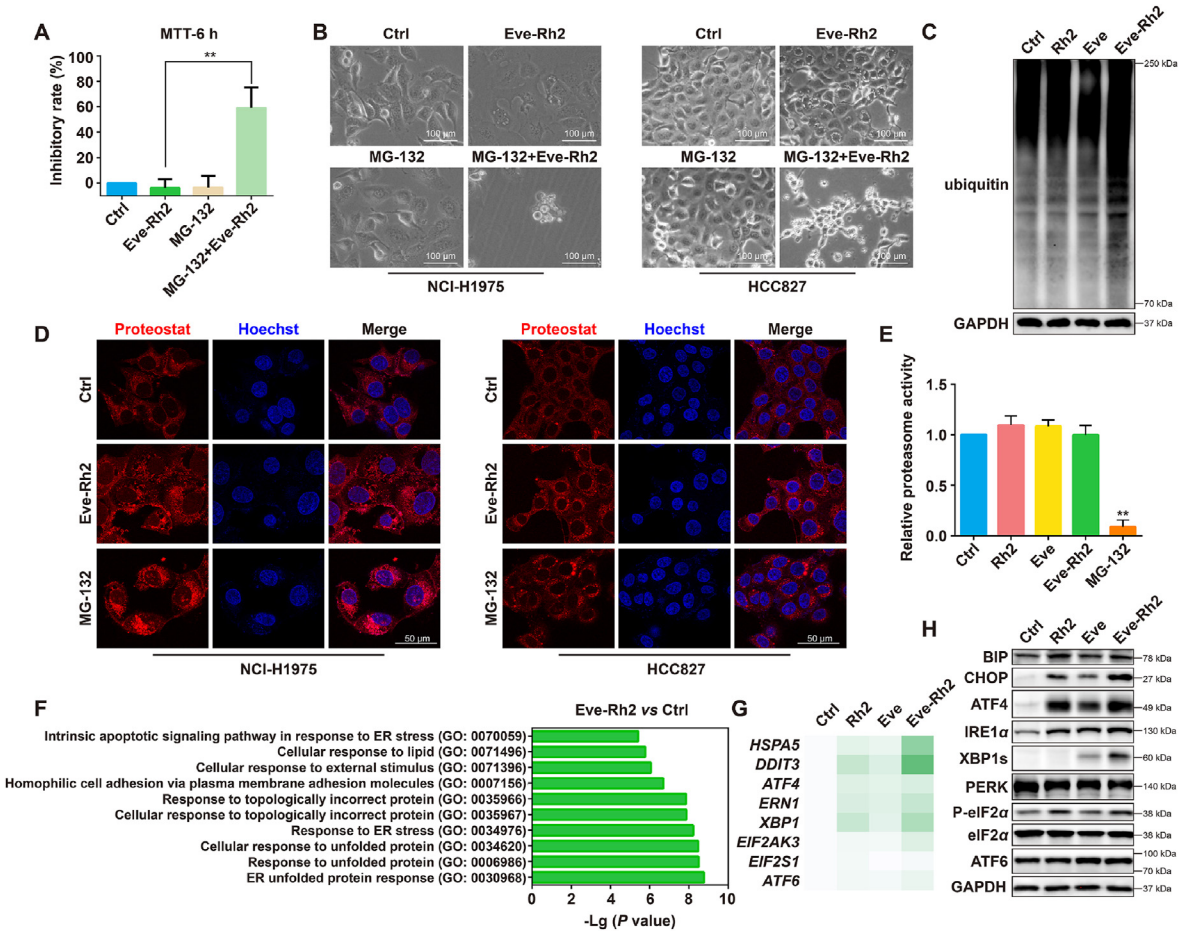

Figure 3 Eve-Rh2 caused the accumulation of protein aggresomes in lung cancer cells. Cells were pretreated with MG-132 (5 μmol/L) and Eve (10 μmol/L) for 1 h and treated with Rh2 (10 μmol/L). (A) Cell viability was determined using MTT assay after treatment for 6 h. Data represent mean ± SD, $n = 3$; $^{**}P < 0.01$. (B) Cell morphology was imaged after treatment for 6 h (scale bar = 100 μm). (C) Expression level of ubiquitin was detected using Western blot after treatment with Rh2 (10 μmol/L), Eve (10 μmol/L), or Eve-Rh2 for 6 h in NCI-H1975 cells. (D) Proteostat Aggresome Detection Kit was used to detect the aggresomes in NCI-H1975 and HCC827 cells after Eve-Rh2 or MG-132 (5 μmol/L) treatment for 6 h. (E) Activity of proteasome was detected using the Proteasome-Glo chymotrypsin-like cell based assay in NCI-H1975 cells after treatment with Rh2 (10 μmol/L), Eve (10 μmol/L), Eve-Rh2, or MG-132 (5 μmol/L) for 6 h. Data are shown as mean ± SD, $n = 3$; $^{**}P < 0.01$ between the tagged group and ctrl group. (F) Gene Ontology analysis was performed on the RNA-Seq data to enrich biological processes after Eve-Rh2 treatment for 6 h. (G) Expression levels of genes related to ER stress were displayed using a heatmap. The color depth represented the expression level. (H) Protein levels of ER stress-related factors were detected using Western blot in NCI-H1975 cells after treatment with Rh2 (10 μmol/L), Eve (10 μmol/L), or Eve-Rh2 for 6 h.

accumulation of protein aggresomes similar with the positive control MG-132 (Fig. 3D), and the phenomenon could be reversed by co-treatment of CHX or A-D (Supporting Information Fig. S8A). These results suggest that Eve-Rh2 induced paraptosis by increasing the accumulation of protein aggresomes. It is well known that MG-132 induces aggresomes accumulation through proteasome inhibition[39]. However, Eve-Rh2 displayed almost no inhibitory effect on the proteasomes (Fig. 3E), implying that Eve-Rh2 induced aggresomes accumulation through a different mechanism. The Gene Ontology analysis suggested that ER stress or unfolded protein response was the main biological process affected by Eve-Rh2 treatment (Fig. 3F), which was highly correlated with the protein aggregation[40,41]. The results of RNA-Seq and Western blot show that the regulatory factors related to ER stress, including BIP, CHOP, ATF4, IRE1α and XBP1s, were up-regulated after Eve-Rh2 treatment (Fig. 3G and H).

3.4. Eve-Rh2 induces the accumulation of P62$^+$ aggresomes leading to paraptosis

Protein aggresomes can be ubiquitinated and recruited to P62 for clearance[42]. Without increased expression of P62 (Fig. 4A and B), Eve-Rh2 triggered the colocalization of P62$^+$ puncta (green) with aggresomes (red) in cancer cells (Fig. 4C). By contrast, P62 was scattered in untreated cells, which had minimal aggresomes. After Eve-Rh2 treatment, the level of P62 in the Triton-X100-insoluble fraction increased, whereas that in the Triton-X100-soluble fraction decreased (Fig. 4D). These data suggest that Eve-Rh2 induced the accumulation of P62$^+$ aggresomes by altering the function

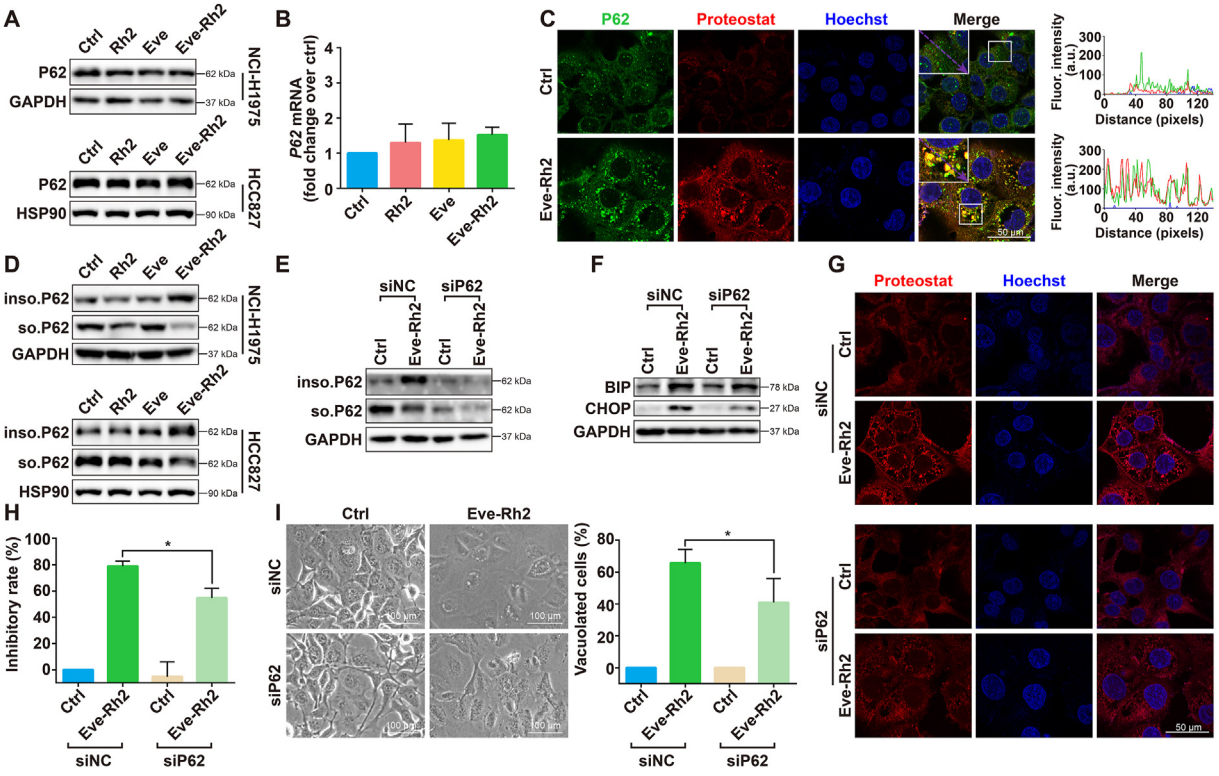

Figure 4 Eve-Rh2-triggered the P62$^+$ aggresomes accumulation induced paraptosis. After Rh2 (10 μmol/L), Eve (10 μmol/L), or Eve-Rh2 treatment for 6 h, the expression level of P62 was determined using (A) Western blot and (B) qRT-PCR. Data represent mean ± SD, $n = 3$. (C) Colocalization of P62 and aggresomes was determined using the immunofluorescence in Eve-Rh2-treated or untreated NCI-H1975 cells after 6 h treatment. Fluorescence intensity was quantified using the Image J software. (D) After Rh2 (10 μmol/L), Eve (10 μmol/L), or Eve-Rh2 treatment for 6 h, the protein levels of P62 in the Triton-X100-soluble and Triton-X100-insoluble fractions were detected using Western blot in NCI-H1975 and HCC827 cells. After transfection with the P62-specific siRNA, NCI-H1975 cells were treated with Eve-Rh2 for 6 h, and the protein levels of (E) insoluble and soluble P62, (F) BIP and CHOP were detected using Western blot. (G) Immunofluorescence assay was performed to analyze the accumulation of aggresomes after Eve-Rh2 treatment for 6 h. (H) Cell viability was detected using MTT assay in NCI-H9175 cells with silenced P62 and Eve-Rh2 treatment for 24 h. Data are shown as mean ± SD, $n = 3$; *$P < 0.05$. (I) Cell morphology was determined after Eve-Rh2 treatment for 6 h (scale bar = 100 μm). The numbers of vacuolated and non-vacuolated cells were counted manually, and the ratio of vacuolated cells was calculated and shown as mean ± SD, $n = 3$; *$P < 0.05$.

and/or the soluble−insoluble form of P62. Thereafter, knockdown of P62 interfered with the accumulation of insoluble P62 (Fig. 4E). As shown in Fig. 4F−I, the interference with P62 accumulation partially reversed Eve-Rh2-induced ER stress, protein aggregation, cell death, and cytoplasmic vacuolation, indicating that the Eve-Rh2-mediated accumulation of P62$^+$ aggresomes triggered paraptosis.

3.5. *TRIB3 mediates the Eve-Rh2-induced accumulation of P62$^+$ aggresomes*

Generally, P62 binds to LC3 in the membranes of autophagosome, thereby mediating the clearance of P62 cargo, containing protein aggresomes[43]. However, the interaction between TRIB3 and P62 leads to the accumulation of P62, and the autophagy-lysosome-dependent degradation is attenuated[44]. The expression level of TRIB3 was significantly increased after Eve-Rh2 treatment, as indicated in the RNA-Seq results (data not shown). Here, Eve-Rh2 increased the protein and mRNA levels of TRIB3 (Fig. 5A and B). TRIB3 and aggresomes were colocalized in the cytosol of Eve-Rh2-treated cells (Fig. 5C). The levels of soluble and insoluble TRIB3 significantly increased after the Eve-Rh2 treatment (Fig. 5D). Interference with the accumulation of insoluble P62 suppressed Eve-Rh2-mediated increase of insoluble TRIB3 (Fig. 5E), and knockdown of TRIB3 reversed Eve-Rh2-induced insoluble P62 accumulation, ER stress, and protein aggregation (Fig. 5F−H). These results suggest that the interaction between TRIB3 and P62 mediated the Eve-Rh2-induced aggresomes accumulation. Furthermore, the knockdown of TRIB3 inhibited Eve-Rh2-caused cell death and cytoplasmic vacuolation (Fig. 5I and J), indicating that the TRIB3-mediated accumulation of aggresomes triggered Eve-Rh2-induced paraptosis.

3.6. *c-MYC mediates the accumulation of TRIB3/P62$^+$ aggresomes via up-regulating the TRIB3 expression*

The IPA was performed on the RNA-Seq data to determine the upstream regulators of TRIB3/P62$^+$ aggresomes accumulation in response to Eve-Rh2 treatment. The top 20 upstream regulators were sorted using the *P* value. Ten transcription regulators, including *NUPR1*, *ATF4*, *JUN*, *NFKB1*, *MYC*, *HIC1*, *XBP1*, *EGR1*, *KLF6* and *RELB*, were enriched (Fig. 6A). The overexpression of *MYC* is usually associated with poor prognosis[45], whereas cells with the higher expression of inducible *MYC* seem

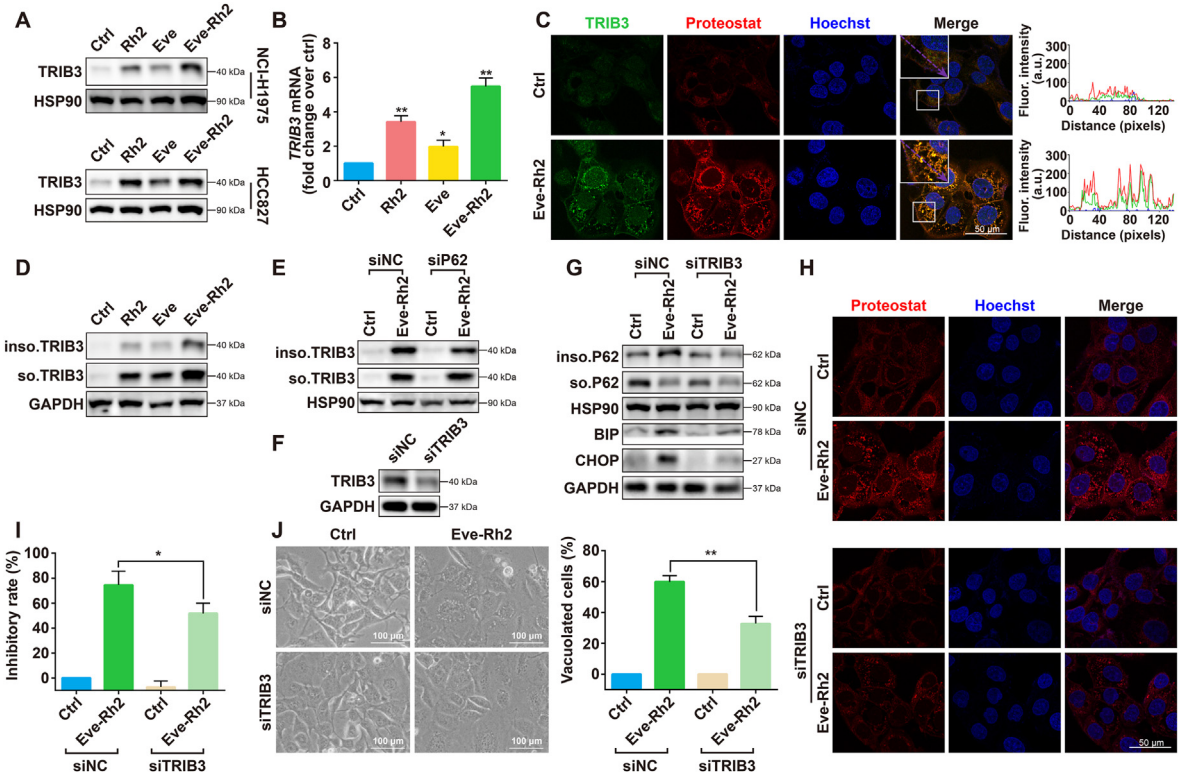

Figure 5 TRIB3-mediated P62^{+} aggresomes accumulation triggered the Eve-Rh2-induced paraptosis. After Rh2 (10 μmol/L), Eve (10 μmol/L), or Eve-Rh2 treatment for 6 h, the expression level of TRIB3 was determined using (A) Western blot and (B) qRT-PCR. Data represent mean ± SD, $n = 3$; $^{*}P < 0.05$ and $^{**}P < 0.01$ between the tagged group and ctrl group. (C) Colocalization of TRIB3 and aggresomes was detected using the immunofluorescence in Eve-Rh2-treated or untreated NCI-H1975 cells after Eve-Rh2 treatment for 6 h. Fluorescence intensity was quantified using the Image J software. Protein levels of insoluble and soluble TRIB3 were determined using Western blot in (D) NCI-H1975 cells treated with Eve-Rh2 for 6 h, and in (E) NCI-H1975 cells with silenced P62 treated with Eve-Rh2 for 6 h. (F) After knockdown of TRIB3, the NCI-H1975 cells were treated with Eve-Rh2. (G) Protein levels of insoluble P62, soluble P62, BIP, and CHOP were detected using Western blot after 6 h of Eve-Rh2 treatment. (H) Aggresomes accumulation was detected using the immunofluorescence after Eve-Rh2 treatment for 6 h. (I) Cell viability was detected using MTT assay after 24 h of Eve-Rh2 treatment. Data are shown as mean ± SD, $n = 3$; $^{*}P < 0.05$. (J) Morphology was imaged after Eve-Rh2 treatment for 6 h (scale bar = 100 μm). The numbers of vacuolated and non-vacuolated cells were counted manually, and the ratio of vacuolated cells was calculated and shown as mean ± SD, $n = 3$; $^{**}P < 0.01$.

more sensitive to the Eve-Rh2 treatment (data not shown). Some studies have reported that c-MYC mediates apoptosis in the absence of growth-stimulating signals[46]. However, whether c-MYC is involved in the regulatory network of paraptosis remains unclear. The IPA network analysis suggested that *MYC* might be an important modulator of the Eve-Rh2 treatment (Fig. 6B). Eve-Rh2 up-regulated the protein and mRNA levels of c-MYC (Fig. 6C and D), and the increased c-MYC located in the nucleus (Fig. 6E). Moreover, the expression level of c-MYC was increased after Eve-Rh2 treatment in tumor tissues, and this finding was consistent with the results of *in vitro* experiments (Fig. 6F). Silencing of c-MYC inhibited the Eve-Rh2-provoked insoluble P62 accumulation, ER stress, protein aggregation, cell death and cytoplasmic vacuolation (Fig. 6G−K). Knockdown of c-MYC also suppressed the Eve-Rh2-up-regulated TRIB3 expression level (Fig. 6L and M), whereas knockdown of TRIB3 did not affect the up-regulation of c-MYC after the Eve-Rh2 treatment (Fig. 6N), indicating that c-MYC was the upstream regulator of TRIB3. These results demonstrate that the Eve-Rh2-induced-c-MYC up-regulation mediated the accumulation of TRIB3/P62^{+} aggresomes by increasing the transcriptional level of TRIB3 and consequently triggered paraptosis.

3.7. Disruption of c-MYC/MAX interaction enhances Eve-Rh2-induced paraptosis

The pMYC-TA-luc plasmid containing several reported c-MYC binding sites (E-box element) was used to determine the classical transcriptional activity of c-MYC after Eve-Rh2 treatment. As shown in Fig. 7A, Eve-Rh2 did not increase the relative luciferase activity of c-MYC, indicating that the E-box binding sites-dependent transcriptional activity of c-MYC was constant after Eve-Rh2 treatment. The c-MYC/MAX interaction inhibitor, 10058-F4, did not reverse the cell death induced by Eve-Rh2 treatment. Instead, 10058-F4 enhanced Eve-Rh2-induced cell death and cytoplasmic vacuolation (Fig. 7B and C), and it exaggerated the Eve-Rh2-mediated accumulation of insoluble TRIB3 and P62 as well as the up-regulation of the TRIB3 mRNA level (Fig. 7D and E). 10074-G5, another inhibitor of c-MYC/MAX interaction, enhanced the Eve-Rh2-induced cytoplasmic vacuolation (Fig. 7F). Eve-Rh2 did not affect the expression level of MAX (Fig. 7G). Knockdown of MAX also enhanced the Eve-Rh2-induced cytoplasmic vacuolation (Fig. 7H and I), which was similar to the phenomenon of Eve-Rh2 plus 10058-F4 or Eve-Rh2 plus 10074-G5 co-treatment. These results indicated that c-MYC

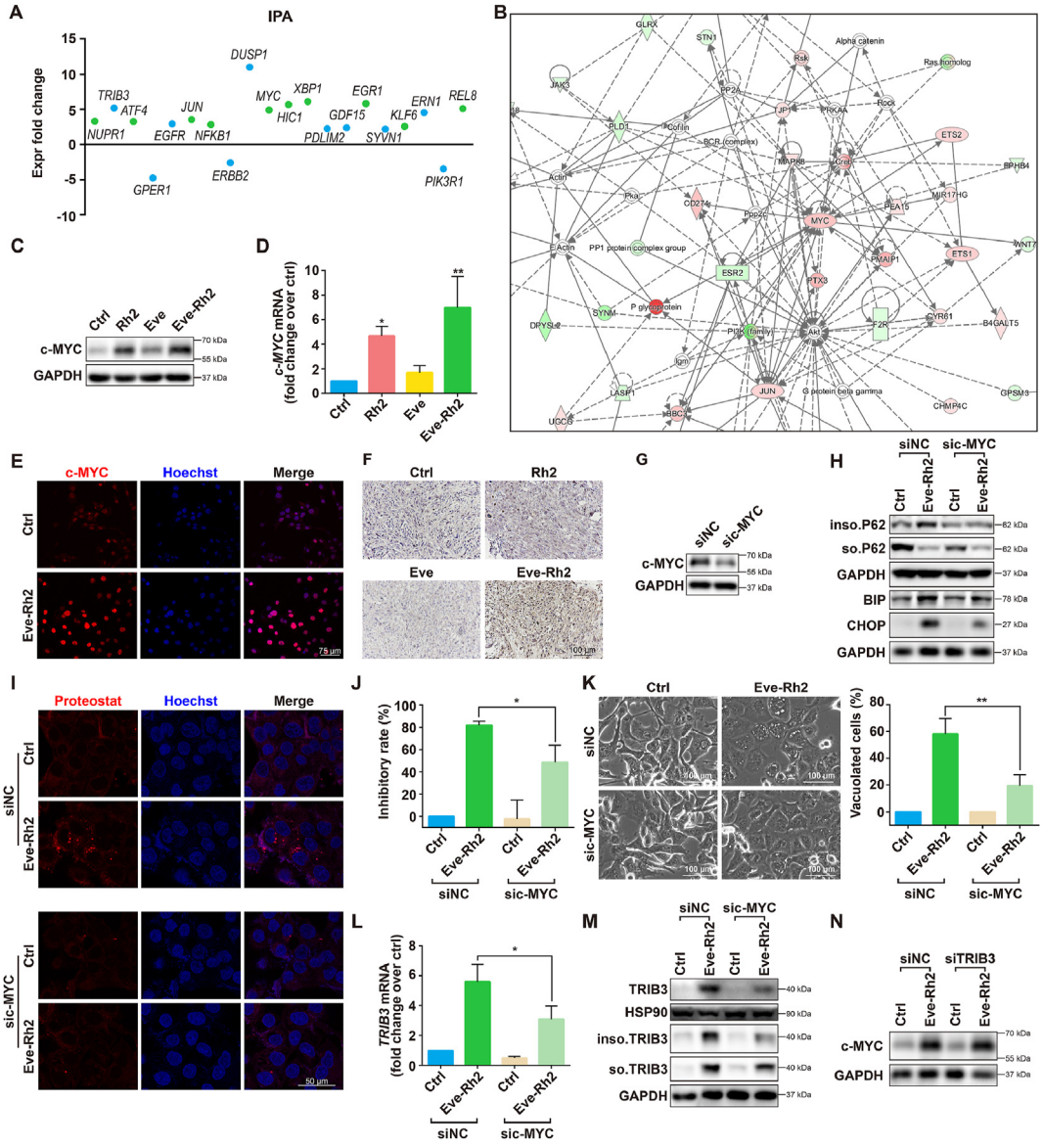

Figure 6 c-MYC mediated the accumulation of TRIB3/P62^{+} aggresomes by up-regulating the TRIB3 expression. (A) Enriched upstream regulators with different expression levels in Ingenuity Pathway Analysis (IPA) were sorted using the *P* value (Eve-Rh2 *vs.* Ctrl). The top 20 regulators were identified, and 10 transcription regulators (green dots) and the other factors (blue dots) were pointed out. (B) Results of IPA network analysis (Eve-Rh2 *vs.* Ctrl). After Rh2 (10 μmol/L), Eve (10 μmol/L), or Eve-Rh2 treatment for 6 h, the expression level of c-MYC was determined using (C) Western blot and (D) qRT-PCR in NCI-H1975 cells. Data represent mean ± SD, $n = 3$; $^{*}P < 0.05$ and $^{**}P < 0.01$ between the tagged group and ctrl group. (E) Localization of c-MYC was detected using the immunofluorescence after Eve-Rh2 treatment for 6 h. (F) Expression level of c-MYC in tumor tissues was detected using immunohistochemical staining. (G) After the silencing of c-MYC, cells were treated with Eve-Rh2. (H) Protein levels of insoluble and soluble P62, BIP and CHOP were determined using Western blot after 6 h of Eve-Rh2 treatment. (I) Aggresomes accumulation was detected using the immunofluorescence after cells were transfected with c-MYC siRNA and treated with Eve-Rh2 for 6 h. (J) Cell viability was detected using MTT assay after Eve-Rh2 treatment for 24 h in cells with silenced c-MYC. Data represent mean ± SD, $n = 3$; $^{*}P < 0.05$. (K) Morphology was imaged after 6 h of Eve-Rh2 treatment (scale bar = 100 μm). The numbers of vacuolated and non-vacuolated cells were counted manually, and the ratio of vacuolated cells was calculated and shown as mean ± SD, $n = 3$; $^{**}P < 0.01$. Expression level of TRIB3 was detected using (L) qRT-PCR and (M) Western blot in NCI-H1975 cells with silenced c-MYC and Eve-Rh2 treatment for 6 h. Data represent mean ± SD, $n = 3$; $^{*}P < 0.05$. (N) Protein level of c-MYC was determined using Western blot in NCI-H1975 cells with silenced TRIB3 and Eve-Rh2 treatment for 6 h.

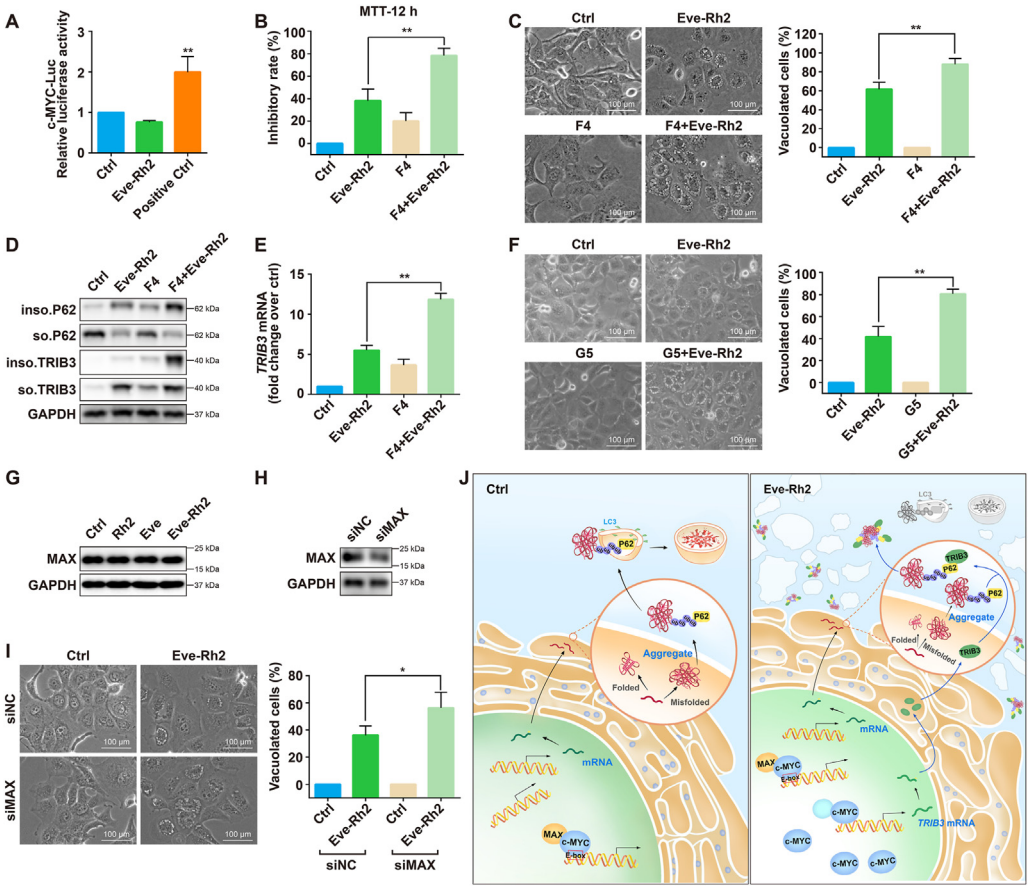

Figure 7 Disruption of the interaction between c-MYC and MAX enhanced the Eve-Rh2-induced paraptosis. (A) NCI-H1975 cells were transfected with the pMYC-TA-luc plasmid, and the relative luciferase activity was detected after the Eve-Rh2 treatment for 6 h. Fetal bovine serum (20%) was used as the positive control of inducing transcriptional activation by c-MYC. Data are shown as mean ± SD, $n = 3$; $^{**}P < 0.01$ between the tagged group and ctrl group. NCI-H1975 cells were pretreated with 10058-F4 (F4, 20 μmol/L) and Eve (10 μmol/L) for 1 h followed by Rh2 (10 μmol/L) treatment. (B) After 12 h treatment, cell viability was detected using MTT assay. Data are shown as mean ± SD, $n = 3$; $^{**}P < 0.01$. (C) After 6 h treatment, the cell morphology was captured (scale bar = 100 μm). The numbers of vacuolated and non-vacuolated cells were counted manually, and the ratio of vacuolated cells was calculated and shown as mean ± SD, $n = 3$; $^{**}P < 0.01$. (D) Protein levels of insoluble and soluble P62, insoluble and soluble TRIB3 were determined using Western blot after treatment for 6 h. (E) The mRNA level of *TRIB3* was detected using qRT-PCR after treatment for 6 h. Data represent mean ± SD, $n = 3$; $^{**}P < 0.01$. (F) Cells were pretreated with 10074-G5 (G5, 10 μmol/L) and Eve (10 μmol/L) for 1 h followed by the Rh2 (10 μmol/L) treatment for another 6 h, and cell morphology was captured (scale bar = 100 μm). The numbers of vacuolated and non-vacuolated cells were counted manually, and the ratio of vacuolated cells was calculated and shown as mean ± SD, $n = 3$; $^{**}P < 0.01$. (G) Expression level of MAX was determined using Western blot in NCI-H1975 cells after treatment with Rh2 (10 μmol/L), Eve (10 μmol/L), or Eve-Rh2 for 6 h. (H) and (I) Cell morphology was captured after knockdown of MAX followed by the treatment with Eve-Rh2 for 6 h (scale bar = 100 μm). The numbers of vacuolated and non-vacuolated cells were counted manually, and the ratio of vacuolated cells was calculated and shown as mean ± SD, $n = 3$; $^{*}P < 0.05$. (J) Schematic of the proposed mechanisms of Eve-Rh2-triggered paraptosis. Protein aggregates containing unfolded or misfolded proteins were ubiquitinated and recruited to P62. In untreated cells (left), the P62 cargo bound to the LC3, which led to the clearance of protein aggresomes. After Eve-Rh2 treatment (right), the expression level of the c-MYC was up-regulated, and the raised c-MYC increased the TRIB3 expression by collaborating with an unknown cofactor. The up-regulated TRIB3 bound to P62, which prevented the interaction between the LC3 and the P62, thereby blocking the degradation of protein aggresomes. The accumulation of protein aggresomes eventually led to cell paraptosis.

mediated the TRIB3 up-regulation and triggered the Eve-Rh2-induced paraptosis through an unclassical c-MYC regulatory network.

4. Discussion

On the grounds of The Cancer Genome Atlas Database, the mTOR pathway is highly active in patients with lung cancer[47]. mTOR is an essential molecule that regulates cell growth, metabolism and survival and a downstream regulator of the EGFR signaling pathway[48]. In addition, the hyperactivated mTOR pathway is a feature of KRAS mutant lung adenocarcinoma after chemotherapy[49]. In this study, we have demonstrated that the combination of Eve (the mTOR inhibitor) and Rh2 exhibits significant anti-lung cancer effect *in vitro* and *in vivo*, not only in EGFR-mutant but also KRAS-mutant lung cancer cells. Eve-Rh2 is more effective in inhibiting tumor growth compared with either Eve monotreatment or Rh2 monotreatment. Moreover, about 30%

mice in the Eve group suffer from mild hepatic fat accumulation, which is one of the major risk factors of nonalcoholic fatty liver disease[50]. In contrary, the mice in the Eve-Rh2 group have no evident liver lesion, indicating that Rh2 attenuates Eve-caused hepatic fat accumulation. Chronic mTOR complex 1 inhibition may lead to hepatic steatosis through persistent induction of the gluconeogenic program in liver[1,51–53]. The hepatic steatosis and hepatotoxicity of Eve has been reported in the clinical case, clinical trials and preclinical study with certain incidence, which may be correlated to Eve-induced glucose and insulin intolerance[27,28,54]. Rh2 has been reported to decrease the plasma glucose[55,56]. In our preliminary study, Rh2 reduced Eve-increased fasting blood glucose level (Supporting Information Fig. S9), suggesting that Rh2 attenuated Eve-caused hepatic fat accumulation might partially through improving the glucose metabolism. Rh2 is the main component of ginseng, which is a tonic and has a long history of clinical application. Rh2 enhances the anti-lung cancer effect of Eve and attenuates its adverse effects, suggesting that Eve-Rh2 is a potential anti-lung cancer candidate and showing the feasibility of incorporating natural products into clinical cancer treatment.

Further study demonstrates that Eve-Rh2 increases the expression level of c-MYC in the process of triggering lung cancer cell death. The sensitivity to Eve-Rh2 treatment seems to be related to the inducible expression level of c-MYC, implying that tumors with highly inducible expressed c-MYC is more likely to benefit from the Eve-Rh2 treatment. As a renowned oncogene, *MYC* is often activated in various cancers, including lung cancer, breast cancer, colon cancer and glioblastomas. Generally, c-MYC functions as a transcription factor, which forms a heterodimer with MAX through a basic-helix-loop-helix leucine-zipper motif and binds to the E-box elements of targeted genes, thereby mediating multiple cellular processes, including cell growth, proliferation, loss of differentiation and apoptosis[57]. In this study, c-MYC mediates the up-regulation of the *TRIB3* mRNA level, leading to the aggresomes accumulation-triggered paraptosis. However, the classical transcriptional activity of c-MYC, which relies on c-MYC/MAX interaction, is not enhanced by the Eve-Rh2 treatment. The inhibitors of c-MYC/MAX interaction and the knockdown of MAX strengthen the Eve-Rh2-induced paraptosis. Therefore, c-MYC up-regulates the TRIB3 transcription level and triggers the Eve-Rh2-induced paraptosis in a new way. The c-MYC/MAX-dependent transcription and tumor malignant development are not activated by the Eve-Rh2-elevated c-MYC when Eve-Rh2 is used for lung cancer treatment. Moreover, the inhibitors of c-MYC/MAX interaction can be added in the regimen of the Eve-Rh2 treatment to further enhance the anti-lung cancer effect of Eve-Rh2. This study provides a treatment strategy for lung cancer, as well as the other cancers with highly inducible expressed *MYC*, through the overactivation of the *MYC* oncogene.

Paraptosis is first described as a non-apoptotic form of programmed cell death in 2000[58], and is characterized by cytoplasmic vacuolation as well as caspase independence and can be reversed by *de novo* protein synthesis inhibitors[15]. The inhibitory effect of protein synthesis inhibitors is often used to determine paraptosis, whereas seldom research has proven the explicit increase in new protein synthesis after treatment with paraptosis inducers. In this study, CHX and A-D reverse the paraptotic morphology induced by the Eve-Rh2 treatment, but Eve-Rh2 does not enhance protein synthesis. Meanwhile, Eve-Rh2 does not affect the proteasome activity, even though the proteasome inhibition is reported to trigger paraptosis[59–61]. Eve-Rh2 causes protein accumulation through mediating the TRIB3/P62^{+} aggresomes formation, which blocks the clearance of the existing unfolded or misfolded proteins, thereby leading to ER stress and ultimately triggering paraptosis. Thus, increased protein synthesis, proteasome inhibition, or aggresomes accumulation eventually leads to protein accumulation, which may be the true executioner of paraptosis.

Furthermore, CHX and A-D suppress the up-regulation of c-MYC and TRIB3 induced by the Eve-Rh2 treatment (Fig. S8B), suggesting that CHX and A-D reverse the Eve-Rh2-induced paraptosis presumably by blocking the up-regulation of c-MYC. Conceivably, c-MYC is the core molecule that mediates the Eve-Rh2-induced paraptosis. As shown in Fig. 7A, Eve-Rh2 does not affect the c-MYC/MAX-dependent transcription, indicating that the elevated c-MYC may collaborate with another uncertain cofactor to induce paraptosis, but the cofactor remains unclear. The two c-MYC inhibitors used in this study (*i.e.*, 10058-F4 and 10074-G5) bind to the basic-helix-loop-helix leucine-zipper domain of c-MYC (the domain to which MAX binds)[62], which enhances the anti-tumor effect of Eve-Rh2. This finding indicates that the inhibitors block the interaction between c-MYC and MAX while do not affect the binding of c-MYC to the cofactor. Therefore, the binding site of the cofactor and c-MYC is presumably different from that of MAX, and the dissociative c-MYC may actively collaborate with this cofactor. Moreover, 10058-F4 alone up-regulated the expression level of TRIB3 and induced the accumulation of insoluble TRIB3 and P62 (Fig. 7D and E), further implying that mediation of TRIB3 expression through collaborating with the cofactor is a novel inherent function of c-MYC. Several cofactors are reported to combine with c-MYC and mediate cellular processes, such as MIZ-1, INI1 and HSF1[46]. HSF1 is a pivotal cofactor of c-MYC in tumorigenesis and positively correlated with the c-MYC expression in hepatocellular carcinoma[63]. Moreover, HSF1 exhibited the potential in regulating TRIB3 expression[64], implying that HSF1 may be involved in the Eve-Rh2-induced paraptosis. The exact cofactor, which cooperates with c-MYC and up-regulates the TRIB3 expression, thereby mediating the accumulation of TRIB3/P62^{+} aggresomes and eventually triggering paraptosis (Fig. 7J), remains to be further explored.

5. Conclusions

Our study indicates for the first time that the protein accumulation is the true executioner of paraptosis. We demonstrate that c-MYC triggers paraptosis by mediating the TRIB3/P62^{+} aggresomes accumulation in an unclassical way. Importantly, dual therapy combining Rh2 with Eve attenuates the hepatic fat accumulation caused by Eve and enhances its anti-cancer effect, shedding new light for the treatment of lung cancer.

Acknowledgments

We would like to appreciate Prof. Hua Li and Ms. Jing Guo (Huazhong University of Science and Technology, China), Prof. Su-Hong Chen and Dr. Bo Li (Zhejiang University of Technology, China) for their assistance in animal experiments, Prof. Cheng-Wei He (University of Macau, China) for sponsoring the P62 antibody, Prof. Jian-Bo Wan (University of Macau, China) for suggestions relating to hepatic fat accumulation, Ms. Xin-Ling He, Mr. Zi-Han Ye and Mr. Wei-Bang Yu (University of Macau, China) for their kind help in animal experiments, and Ms. Hai-Lu Su (China

Academy of Art, China) for her assistance in drawing Fig. 7J. In addition, we thank the members of the SPF animal facility of Faculty of Health Sciences at the University of Macau for experimental and technical supports. This study was supported by the National Natural Science Foundation of China (No. 81973516) and partially supported by the Science and Technology Development Fund, Macao S.A.R, China (Nos. 024/2016/A1 and 0129/2019/A3), as well as University of Macau (No. CPG2021-00022-ICMS).

Author contributions

Min-Xia Su: Conceptualization, Methodology, Investigation, Data curation, Writing - original draft, Writing - review & editing; Yu-Lian Xu: Methodology, Investigation, Data curation, Writing - review & editing; Xiao-Ming Jiang: Methodology, Investigation, Data curation; Mu-Yang Huang: Methodology, Investigation, Data curation, Writing - review & editing; Le-Le Zhang: Methodology, Data curation; Luo-Wei Yuan: Methodology, Data curation; Xiao-Huang Xu: Investigation, Data curation. Qi Zhu: Methodology, Data curation; Jian-Li Gao: Methodology, Data curation; Jia-Hong Lu: Methodology, Writing - review & editing; Xiuping Chen: Data curation, Writing - review & editing; Ming-Qing Huang: Natural products contribution, Data curation; Yitao Wang: Writing - review & editing; Jin-Jian Lu: Conceptualization, Methodology, Data curation, Supervision, Project administration, Funding acquisition, Writing - review & editing.

Conflicts of interest

The authors declare no conflict of interest, financial or otherwise.

Appendix A. Supporting information

Supporting data to this article can be found online at https://doi.org/10.1016/j.apsb.2021.09.014.

References

1. Saxton RA, Sabatini DM. mTOR signaling in growth, metabolism, and disease. *Cell* 2017;**168**:960−76.
2. Feng FF, Cheng P, Sun C, Wang H, Wang W. Inhibitory effects of polyphyllins I and VII on human cisplatin-resistant NSCLC *via* p53 upregulation and CIP2A/AKT/mTOR signaling axis inhibition. *Chin J Nat Med* 2019;**17**:768−77.
3. Swanton C, Govindan R. Clinical implications of genomic discoveries in lung cancer. *N Engl J Med* 2016;**374**:1864−73.
4. Conciatori F, Ciuffreda L, Bazzichetto C, Falcone I, Pilotto S, Bria E, et al. mTOR cross-talk in cancer and potential for combination therapy. *Cancers (Basel)* 2018;**10**:23.
5. Ou SH, Moon J, Garland LL, Mack PC, Testa JR, Tsao AS, et al. SWOG S0722: phase II study of mTOR inhibitor everolimus (RAD001) in advanced malignant pleural mesothelioma (MPM). *J Thorac Oncol* 2015;**10**:387−91.
6. Wang CZ, Anderson S, Du W, He TC, Yuan CS. Red ginseng and cancer treatment. *Chin J Nat Med* 2016;**14**:7−16.
7. Wong AS, Che CM, Leung KW. Recent advances in ginseng as cancer therapeutics: a functional and mechanistic overview. *Nat Prod Rep* 2015;**32**:256−72.
8. Li X, Chu S, Lin M, Gao Y, Liu Y, Yang S, et al. Anticancer property of ginsenoside Rh2 from ginseng. *Eur J Med Chem* 2020;**203**:112627.
9. Huang Q, Wang Q, Li D, Wei X, Jia Y, Zhang Z, et al. Co-administration of 20(*S*)-protopanaxatriol (g-PPT) and EGFR-TKI overcomes EGFR-TKI resistance by decreasing SCD1 induced lipid accumulation in non-small cell lung cancer. *J Exp Clin Cancer Res* 2019;**38**:129.
10. Pak JN, Jung JH, Park JE, Hwang J, Lee HJ, Shim BS, et al. p53 dependent LGR5 inhibition and caspase 3 activation are critically involved in apoptotic effect of compound K and its combination therapy potential in HCT116 cells. *Phytother Res* 2020;**34**:2745−55.
11. Liu GW, Liu YH, Jiang GS, Ren WD. The reversal effect of Ginsenoside Rh2 on drug resistance in human colorectal carcinoma cells and its mechanism. *Hum Cell* 2018;**31**:189−98.
12. Lee H, Lee S, Jeong D, Kim SJ. Ginsenoside Rh2 epigenetically regulates cell-mediated immune pathway to inhibit proliferation of MCF-7 breast cancer cells. *J Ginseng Res* 2018;**42**:455−62.
13. Wang M, Yan SJ, Zhang HT, Li N, Liu T, Zhang YL, et al. Ginsenoside Rh2 enhances the antitumor immunological response of a melanoma mice model. *Oncol Lett* 2017;**13**:681−5.
14. Petrillo S, Chiabrando D, Genova T, Fiorito V, Ingoglia G, Vinchi F, et al. Heme accumulation in endothelial cells impairs angiogenesis by triggering paraptosis. *Cell Death Differ* 2018;**25**:573−88.
15. Sperandio S, Poksay K, de Belle I, Lafuente MJ, Liu B, Nasir J, et al. Paraptosis: mediation by MAP kinases and inhibition by AIP-1/Alix. *Cell Death Differ* 2004;**11**:1066−75.
16. Lee D, Kim IY, Saha S, Choi KS. Paraptosis in the anti-cancer arsenal of natural products. *Pharmacol Ther* 2016;**162**:120−33.
17. Chen X, Chen X, Zhang X, Wang L, Cao P, Rajamanickam V, et al. Curcuminoid B63 induces ROS-mediated paraptosis-like cell death by targeting TrxR1 in gastric cells. *Redox Biol* 2019;**21**:101061.
18. Kim IY, Shim MJ, Lee DM, Lee AR, Kim MA, Yoon MJ, et al. Loperamide overcomes the resistance of colon cancer cells to bortezomib by inducing CHOP-mediated paraptosis-like cell death. *Biochem Pharmacol* 2019;**162**:41−54.
19. Mohamed E, Sierra RA, Trillo-Tinoco J, Cao Y, Innamarato P, Payne KK, et al. The unfolded protein response mediator PERK governs myeloid cell-driven immunosuppression in tumors through inhibition of STING signaling. *Immunity* 2020;**52**:668−82. e7.
20. Hetz C, Zhang K, Kaufman RJ. Mechanisms, regulation and functions of the unfolded protein response. *Nat Rev Mol Cell Biol* 2020;**21**:421−38.
21. Roy A, Kumar A. ER stress and unfolded protein response in cancer cachexia. *Cancers (Basel)* 2019;**11**:1929.
22. Jiang XM, Xu YL, Yuan LW, Zhang LL, Huang MY, Ye ZH, et al. TGFβ2-mediated epithelial−mesenchymal transition and NF-κB pathway activation contribute to osimertinib resistance. *Acta Pharmacol Sin* 2021;**42**:451−9.
23. Nogova L, Mattonet C, Scheffler M, Taubert M, Gardizi M, Sos ML, et al. Sorafenib and everolimus in patients with advanced solid tumors and KRAS-mutated NSCLC: a phase I trial with early pharmacodynamic FDG-PET assessment. *Cancer Med* 2020;**9**:4991−5007.
24. Jin ZH, Qiu W, Liu H, Jiang XH, Wang L. Enhancement of oral bioavailability and immune response of ginsenoside Rh2 by co-administration with piperine. *Chin J Nat Med* 2018;**16**:143−9.
25. Chen YC, Huang MY, Zhang LL, Feng ZL, Jiang XM, Yuan LW, et al. Nagilactone E increases PD-L1 expression through activation of c-Jun in lung cancer cells. *Chin J Nat Med* 2020;**18**:517−25.
26. Ruzzolini J, Peppicelli S, Andreucci E, Bianchini F, Margheri F, Laurenzana A, et al. Everolimus selectively targets vemurafenib resistant BRAF(V600E) melanoma cells adapted to low pH. *Cancer Lett* 2017;**408**:43−54.
27. Schieren G, Bölke E, Scherer A, Raffel A, Gerber PA, Kröpil P, et al. Severe everolimus-induced steatohepatis: a case report. *Eur J Med Res* 2013;**18**:22.
28. Kim SJ, Kang HJ, Kim JS, Eom HS, Huh J, Ko YH, et al. A phase I study of everolimus and CHOP in newly diagnosed peripheral T-cell lymphomas. *Invest New Drugs* 2013;**31**:1514−21.
29. Nieto N, Rojkind M. Repeated whiskey binges promote liver injury in rats fed a choline-deficient diet. *J Hepatol* 2007;**46**:330−9.
30. Caldwell S, Ikura Y, Dias D, Isomoto K, Yabu A, Moskaluk C, et al. Hepatocellular ballooning in NASH. *J Hepatol* 2010;**53**:719−23.

31. Lohr JW, Willsky GR, Acara MA. Renal drug metabolism. *Pharmacol Rev* 1998;**50**:107−41.
32. Seo MJ, Lee DM, Kim IY, Lee D, Choi MK, Lee JY, et al. Gambogic acid triggers vacuolization-associated cell death in cancer cells *via* disruption of thiol proteostasis. *Cell Death Dis* 2019;**10**:187.
33. Yoon MJ, Kim EH, Lim JH, Kwon TK, Choi KS. Superoxide anion and proteasomal dysfunction contribute to curcumin-induced paraptosis of malignant breast cancer cells. *Free Radic Biol Med* 2010;**48**:713−26.
34. Li B, Zhao J, Wang CZ, Searle J, He TC, Yuan CS, et al. Ginsenoside Rh2 induces apoptosis and paraptosis-like cell death in colorectal cancer cells through activation of p53. *Cancer Lett* 2011;**301**:185−92.
35. Baraz R, Cisterne A, Saunders PO, Hewson J, Thien M, Weiss J, et al. mTOR inhibition by everolimus in childhood acute lymphoblastic leukemia induces caspase-independent cell death. *PLoS One* 2014;**9**: e102494.
36. Addi C, Presle A, Frémont S, Cuvelier F, Rocancourt M, Milin F, et al. The Flemmingsome reveals an ESCRT-to-membrane coupling *via* ALIX/syntenin/syndecan-4 required for completion of cytokinesis. *Nat Commun* 2020;**11**:1941.
37. Lee JA, Beigneux A, Ahmad ST, Young SG, Gao FB. ESCRT-III dysfunction causes autophagosome accumulation and neurodegeneration. *Curr Biol* 2007;**17**:1561−7.
38. Loi M, Molinari M. Mechanistic insights in recov-ER-phagy: micro-ER-phagy to recover from stress. *Autophagy* 2020;**16**:385−6.
39. Wan Y, Yang Z, Guo J, Zhang Q, Zeng L, Song W, et al. Misfolded Gβ is recruited to cytoplasmic dynein by Nudel for efficient clearance. *Cell Res* 2012;**22**:1140−54.
40. Verwilst P, Kim K, Sunwoo K, Kim HR, Kang C, Kim JS. Revealing protein aggregates under thapsigargin-induced ER stress using an ER-targeted thioflavin. *ACS Sens* 2019;**4**:2858−63.
41. Cui Y, Parashar S, Zahoor M, Needham PG, Mari M, Zhu M, et al. A COPII subunit acts with an autophagy receptor to target endoplasmic reticulum for degradation. *Science* 2019;**365**:53−60.
42. Chen Y, Li Q, Li Q, Xing S, Liu Y, Liu Y, et al. p62/SQSTM1, a central but unexploited target: advances in its physiological/pathogenic functions and small molecular modulators. *J Med Chem* 2020;**63**:10135−57.
43. Rogov V, Dötsch V, Johansen T, Kirkin V. Interactions between autophagy receptors and ubiquitin-like proteins form the molecular basis for selective autophagy. *Mol Cell* 2014;**53**:167−78.
44. Hua F, Li K, Yu JJ, Hu ZW. The TRIB3-SQSTM1 interaction mediates metabolic stress-promoted tumorigenesis and progression *via* suppressing autophagic and proteasomal degradation. *Autophagy* 2015;**11**:1929−31.
45. Pelengaris S, Khan M, Evan G. c-MYC: more than just a matter of life and death. *Nat Rev Cancer* 2002;**2**:764−76.
46. Caforio M, Sorino C, Iacovelli S, Fanciulli M, Locatelli F, Folgiero V. Recent advances in searching c-Myc transcriptional cofactors during tumorigenesis. *J Exp Clin Cancer Res* 2018;**37**:239.
47. Crees ZD, Shearrow C, Lin L, Girard J, Arasi K, Bhoraskar A, et al. EGFR/c-Met and mTOR signaling are predictors of survival in non-small cell lung cancer. *Ther Adv Med Oncol* 2020;**12**. 1758835920953731.
48. Abraham RT, Gibbons JJ. The mammalian target of rapamycin signaling pathway: twists and turns in the road to cancer therapy. *Clin Cancer Res* 2007;**13**:3109−14.
49. Liang SQ, Bührer ED, Berezowska S, Marti TM, Xu D, Froment L, et al. mTOR mediates a mechanism of resistance to chemotherapy and defines a rational combination strategy to treat KRAS-mutant lung cancer. *Oncogene* 2019;**38**:622−36.
50. Targher G, Byrne CD. Non-alcoholic fatty liver disease: an emerging driving force in chronic kidney disease. *Nat Rev Nephrol* 2017;**13**: 297−310.
51. Houde VP, Brûlé S, Festuccia WT, Blanchard PG, Bellmann K, Deshaies Y, et al. Chronic rapamycin treatment causes glucose intolerance and hyperlipidemia by upregulating hepatic gluconeogenesis and impairing lipid deposition in adipose tissue. *Diabetes* 2010;**59**:1338−48.
52. Li C, Jones PM, Persaud SJ. Role of the endocannabinoid system in food intake, energy homeostasis and regulation of the endocrine pancreas. *Pharmacol Ther* 2011;**129**:307−20.
53. Gomes P, Fleming Outeiro T, Cavadas C. Emerging role of sirtuin 2 in the regulation of mammalian metabolism. *Trends Pharmacol Sci* 2015; **36**:756−68.
54. Chang GR, Hou PH, Wang CM, Wu CF, Su HK, Liao HJ, et al. Chronic everolimus treatment of high-fat diet mice leads to a reduction in obesity but impaired glucose tolerance. *Pharmacol Res Perspect* 2021;**9**:e00732.
55. Lai DM, Tu YK, Liu IM, Chen PF, Cheng JT. Mediation of beta-endorphin by ginsenoside Rh2 to lower plasma glucose in streptozotocin-induced diabetic rats. *Planta Med* 2006;**72**:9−13.
56. Lee WK, Kao ST, Liu IM, Cheng JT. Increase of insulin secretion by ginsenoside Rh2 to lower plasma glucose in Wistar rats. *Clin Exp Pharmacol Physiol* 2006;**33**:27−32.
57. Kress TR, Sabò A, Amati B. MYC: connecting selective transcriptional control to global RNA production. *Nat Rev Cancer* 2015;**15**: 593−607.
58. Sperandio S, de Belle I, Bredesen DE. An alternative, nonapoptotic form of programmed cell death. *Proc Natl Acad Sci U S A* 2000;**97**: 14376−81.
59. Yoon MJ, Kang YJ, Lee JA, Kim IY, Kim MA, Lee YS, et al. Stronger proteasomal inhibition and higher CHOP induction are responsible for more effective induction of paraptosis by dimethoxycurcumin than curcumin. *Cell Death Dis* 2014;**5**:e1112.
60. Yoon MJ, Kim EH, Kwon TK, Park SA, Choi KS. Simultaneous mitochondrial Ca^{2+} overload and proteasomal inhibition are responsible for the induction of paraptosis in malignant breast cancer cells. *Cancer Lett* 2012;**324**:197−209.
61. Nedungadi D, Binoy A, Pandurangan N, Pal S, Nair BG, Mishra N. 6-Shogaol induces caspase-independent paraptosis in cancer cells *via* proteasomal inhibition. *Exp Cell Res* 2018;**364**:243−51.
62. Hammoudeh DI, Follis AV, Prochownik EV, Metallo SJ. Multiple independent binding sites for small-molecule inhibitors on the oncoprotein c-Myc. *J Am Chem Soc* 2009;**131**:7390−401.
63. Cigliano A, Pilo MG, Li L, Latte G, Szydlowska M, Simile MM, et al. Deregulated c-Myc requires a functional HSF1 for experimental and human hepatocarcinogenesis. *Oncotarget* 2017;**8**: 90638−50.
64. Hensen SM, Heldens L, van Enckevort CM, van Genesen ST, Pruijn GJ, Lubsen NH. Heat shock factor 1 is inactivated by amino acid deprivation. *Cell Stress Chaperones* 2012;**17**:743−55.